



HAL
open science

Probabilistic metamodels to quantify uncertainties in electric powertrain whining noise contribution

Vinay Prakash, Olivier Sauvage, Jérôme Antoni, L. Gagliardini

► **To cite this version:**

Vinay Prakash, Olivier Sauvage, Jérôme Antoni, L. Gagliardini. Probabilistic metamodels to quantify uncertainties in electric powertrain whining noise contribution. 2022. hal-04596693

HAL Id: hal-04596693

<https://hal.science/hal-04596693>

Preprint submitted on 11 Jun 2024

HAL is a multi-disciplinary open access archive for the deposit and dissemination of scientific research documents, whether they are published or not. The documents may come from teaching and research institutions in France or abroad, or from public or private research centers.

L'archive ouverte pluridisciplinaire **HAL**, est destinée au dépôt et à la diffusion de documents scientifiques de niveau recherche, publiés ou non, émanant des établissements d'enseignement et de recherche français ou étrangers, des laboratoires publics ou privés.

Probabilistic metamodels to quantify uncertainties in electric powertrain whining noise contribution

Vinay Prakash^{1,2}, Olivier Sauvage¹, Laurent Gagliardini³, Jérôme Antoni²

¹Stellantis N.V., 2 Bd de l'Europe, Poissy, France

²Univ Lyon, INSA Lyon, LVA, EA677, 69621 Villeurbanne, France

³Stellantis N.V., NVH Département, Vélizy-Villacoublay

Abstract

With electromobility, vehicles are becoming quieter due to the presence of electric motors that replace internal combustion engines. The interior cabin noise of electric vehicles is characterized by high-frequency components that can be annoying and unpleasant. Therefore, it is essential to analyse the NVH behaviour of e-powertrains early in the design-phase. However, this induces inherent uncertainties during the design process related to the operating conditions, geometrical parameters, measurement techniques, etc. that need to be quantified with fast and comprehensive stochastic models.

In this work, we first present a deterministic framework to provide first-order estimations of the e-powertrain's interior whining noises, combining both the airborne & structure-borne contribution with data-driven NVH transfers meta-models. Subsequently, stochasticity is induced in the deterministic models considering random sampling of operating conditions and the chosen geometrical parameters for the e-machine under assessment. At each stage, metamodels (or surrogates), developed in the Bayesian framework, take into account the uncertainties which are propagated from operating conditions to whining noise contribution inside the cabin. The work is demonstrated on an interior permanent magnet synchronous motor which is widely used in electric vehicles traction drives.

Introduction

Due to an upshift of concerns regarding climate change and sustainable future, European union have decided to go net zero-emission by 2035 implying a possible ban on ICE vehicles. This would make electric vehicles (EVs) fleets expand at a rapid pace which is already doubling with each passing year [1]. Consequently, automakers are shifting their focus towards conceptualizing and improving various EV characteristics as per customer's comfort and needs.

Noise, vibration and harshness (NVH) is one of the key criteria that significantly affects customer's perception of quality and an overall image of the vehicle. Due to the absence of ICE, EVs are much quieter but have a different acoustic signature. The interior noise contribution has high-frequency tonal components (also known as whining noise) that are usually perceived as rather annoying and unpleasant [2]. The major sources of interior noise in EVs can still be broadly classified under three categories namely, aerodynamic noise, tire-pavement interaction noise, and e-powertrain noise. The first two contributions make up the background (or masking) noise and the main source of whining (tonal) comes from the electrified powertrains. Noises originating from e-powertrains are mostly of mechanical (for e.g., gear meshing, shaft misalignment, etc.), aerodynamic (flow of ventilating air through and over the motor), and electromagnetic origins (due to electromagnetic interaction) [3].

Page 1 of 11

Permanent Magnet Synchronous Motors (PMSM) have been widely used in EVs for traction application due to their high torque to inertia and volume ratio, high efficiency, better dynamic performance as compared to motors with electromagnetic excitation, and its simplicity in design, construction and maintenance [4].

A lot of research work has already been published to predict the whining noise contribution in PMSMs due to electromagnetic field effects. Review articles [4,5] provide detailed information on different methods for prediction and mitigation of noise in electrical machines. During the vehicle development phase, the interior acoustic levels can be predicted with desired accuracy using complex structural-acoustics computational models based on 3D finite elements, which is usually time-consuming. Also, in order to capture the random behavior due to various operating conditions, and unknown design parameter space, an NVH designer must deal with challenging levels of uncertainties during early-stage design as no precise (or unique) information is available regarding the design parameters. Therefore, a robust framework is needed that would combine the available prior knowledge in the form of measured/simulated data or domain-expert knowledge with numerical (or analytical) models. For quick evaluation of design alternatives and assess uncertainties, stochastic surrogate models or meta-models are generally preferred, where the output response is depicted by the probability distribution.

Metamodels are not so new in engineering design community. They have been extensively used as "cheap", yet robust approximations of the functional relationship between the input parameters and the output responses [6]. In automotive NVH domain, different metamodels have been employed to achieve minimal engine noise inside the cabin, optimal vehicle mass, learning an aerodynamic wind-noise model, etc. Readers are encouraged to go through [7] to review different metamodeling techniques. In the context of e-machine acoustics, Wang *et al.* [8] proposed a neural network-based noise prediction of e-motor where the surrogate model was built to predict the natural frequencies of the stator. Similarly, in [9], Mohammadi *et al.* used three neural networks to predict the average torque, the torque ripple and sound pressure level (SPL) for multi-objective optimization. In another study [10], multiple surrogate models were compared to predict the acoustic noise of PMSMs. Despite such deterministic developments, not much has been studied in the scientific community to consider the uncertainties in PMSMs acoustic responses. As the electromagnetic excitations in e-machines can be sensitive to even slight variations of the geometric and control parameters of the active magnetic parts, it is important to consider such variations in the output predictions. Notably, Jeannerot *et al.* [11] performed an FEM based probabilistic robust optimization on a PMSM to minimize the SPL, which proved to be time-consuming when the variability of random parameters was considered. In [12], Pulido *et al.* built a Gaussian process surrogate model of PMSM based on nonlinear FEM to account for uncertainty in torque, flux

linkage and core loss. As can be noted, in all previous works, SPL assessment was made only for the PMSM without considering the different transfer paths leading to the interior cabin noise. Therefore, the “global” perspective of such metamodels with uncertain parameters in EVs was missing, which is addressed in this paper.

With respect to the noise assessment, a typical global scheme, as shown in Figure 1, can be considered where the SPL perceived inside the cabin is dependent on several parameters such as the operating conditions, for instance, the speed of the vehicle, and comes from electromagnetic whine along with the broadband masking noise. Different key performance indicators can then be estimated as final outputs, for instance, prominence ratio resulting in prominent tones in the SPL spectra. In a recent article [13], Prakash *et al.* developed Bayesian surrogates to consider such background noises (dashed blue box in Figure 1) using measurement databases. Therefore, the focus of this article is on building the probabilistic surrogate for electromagnetic whine i.e., the dashed red box in Figure 1 which will be detailed in the next subsection.

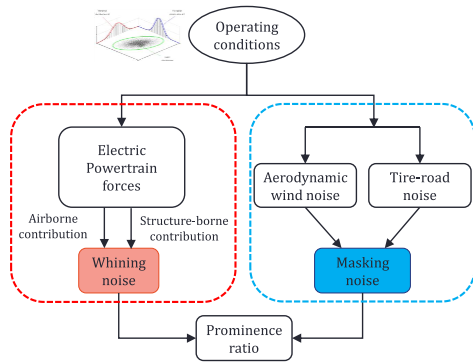


Figure 1. Global scheme to predict interior cabin noise due to three major sources (aerodynamic wind, tire-road interaction, and electromagnetic whine)

Due to the complexity of interior cabin SPL assessment involving interaction between different physical mechanisms and design parameters, a certain level of assumptions/simplifications are necessary to set the scope of this article. In this study, interior-IPMSM (IPMSM) is used in which the permanent magnets are embedded in the rotor core. The mechanical (for e.g., gear whine) and aerodynamic noises are not considered for the sake of simplicity, but the same methodological framework applies. In addition, since the structure-borne contribution is more challenging than airborne, it will be the focus of this study. Besides, global surrogates are modeled within Bayesian framework to account for the uncertainty in whining noise prediction for EVs during early-stage NVH design. Bayesian approach has been specifically chosen as it allows to stochastically quantify the uncertainties considering prior knowledge on the uncertain parameters.

Deterministic assessment of whining noise contribution

Focusing only on the dashed red box from Figure 1, the whining noise assessment due to electromagnetic interaction within IPMSMs involves an interplay between different weakly-coupled physical mechanisms as shown in Figure 2.

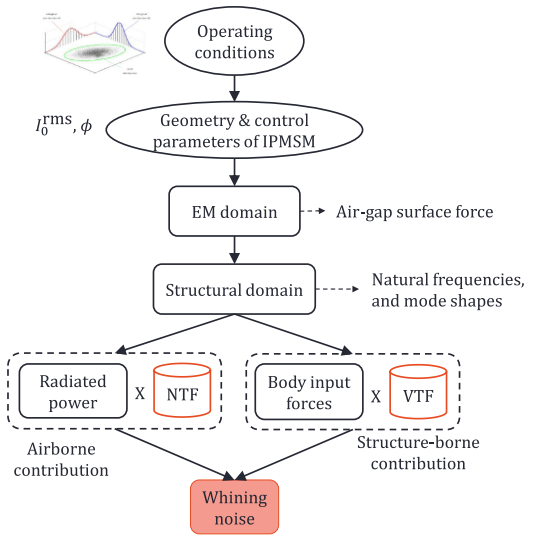


Figure 2. Overview of the multi-physical mechanism involved in the generation of whining noise in EVs (EM stands for electromagnetic)

Each block of the flowchart is described as follows:

- Operating conditions (OC) are typically the client usage profiles or driving conditions that are collected in real driving conditions. They are represented by pairs of (Ω, τ) with Ω being the motor speed in [RPM] and τ being the wheel torque in [Nm]. Their distribution is known a priori.
- IPMSMs are generally fed with 3-phase sinusoidal currents. Therefore, the control parameters consist of input current pairs (I_0^{rms}, ϕ) where, I_0^{rms} is the root-mean-square amplitude of the current and ϕ is its phase angle in electrical degrees. They can also be fed with currents with high order harmonics but are not considered in this study. Along with control parameters, each IPMSM is characterized by its geometrical design parameters (see Figure 3) for instance, length, outer radius, and inner radius of stator.

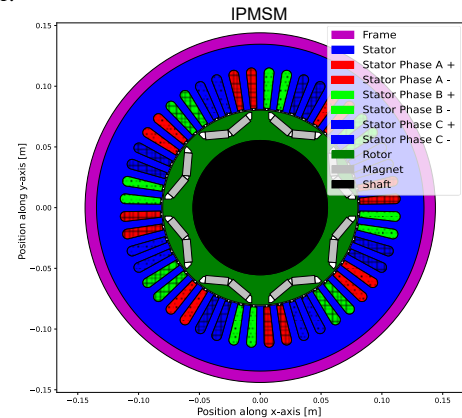


Figure 3. Typical full 2D-model of an IPMSM showing different parts

- The electromagnetic (EM) domain is then solved to get the magnetic flux densities in the airgap. This can be obtained using numerical, semi-analytical, and analytical methods. Analytically, the magnetic flux densities in the airgap can be estimated using magnetomotive force function and a permeance function [3]. Numerical and semi-analytical methods make use of the vector potential approach within FE framework to solve

the magnetic problem. In this work, 2D-FE model of an IPMSM is realized using open-source FEMM coupled with Pyleecan [14]. The magnetostatic problem is solved for each rotor position exploiting the symmetry along the edges and reducing it to 1/8th sector of the full model, as can be seen in Figure 4. The Maxwell pressure (also referred to as airgap surface force (AGSF)) in [N/m²] applying on the stator core along the airgap (δ) is given by [3]:

$$P_{\text{rad}}(R_\delta, \theta, t) = -\frac{1}{2\mu_0} \left(B_{\text{rad}}^2(R_\delta, \theta, t) - B_{\text{tan}}^2(R_\delta, \theta, t) \right), \quad (1)$$

$$P_{\text{tan}}(R_\delta, \theta, t) = -\frac{1}{2\mu_0} (B_{\text{rad}}(R_\delta, \theta, t)B_{\text{tan}}(R_\delta, \theta, t)), \quad (2)$$

where, “rad” and “tan” denote the radial and tangential components, respectively. R_δ is the radius at which the pressure components are computed. It is usually computed in the middle of the airgap. B is the magnetic flux density in [T], μ_0 is the magnetic permeability of vacuum, $\theta \in [0, 2\pi[$ is the angular position, and t is time. Taking the Fourier transform in both time and space, we can represent the Maxwell pressure as:

$$P_{\text{rad}}(R_\delta, \theta, t) = \sum_{r=0, s=-\infty}^{+\infty} \hat{P}_{r,s}^{\text{rad}} \exp(r\theta \pm s\omega_e t + \phi_{r,s}^{\text{rad}}), \quad (3)$$

$$P_{\text{tan}}(R_\delta, \theta, t) = \sum_{r=0, s=-\infty}^{+\infty} \hat{P}_{r,s}^{\text{tan}} \exp(r\theta \pm s\omega_e t + \phi_{r,s}^{\text{tan}}), \quad (4)$$

where, r is the spatial order of the force with respect to θ which determines the periodic shape of the force distribution, s is the temporal order with respect to the mechanical frequency ω_e , and $\phi_{r,s}$ is the phase information associated with each harmonic. The angular velocity of rotor in electrical degree is given by $\omega_e = 2\pi f_e$, where f_e is the fundamental stator winding electrical frequency. With N_{pp} being the number of pole-pairs and Ω the rotational speed in RPM, the electrical frequency is given by $f_e = \frac{\Omega}{60} N_{pp}$. In this article, a progressive wave of spatial order r and frequency f_e is denoted by a pair (r, sf_e) .

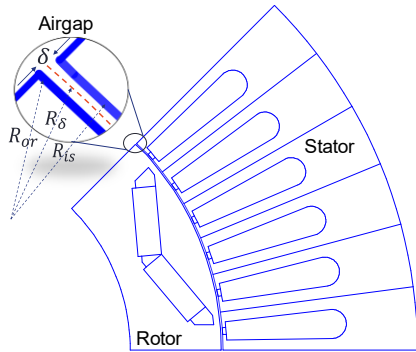


Figure 4. 1/8-th sector of IPMSM showing the boundary at which AGSF is computed (R_{or} : rotor outer radius, R_{is} : stator inner radius, R_δ : airgap radius)

- In structural domain, the dynamic response of the stator is calculated by modal frequency response. The excitations coming from the EM-domain are first transformed from time-domain to frequency domain and are then mapped on to the structural mesh using a mapping tool [11]. This can easily be achieved using commercially available FE solvers as is done in many previous

studies [2,15]. Despite being more accurate than analytical or semi-analytical methods, numerical methods are time-consuming and prediction on wide-speed range becomes a challenge [4]. Therefore, a common technique is to go semi-analytical by calculating the EM force through FEM and then vibration and acoustic prediction can be obtained using analytical approaches [16]. Calculation of natural frequencies and mode shapes of a simplified full stator system is covered in the next sub-section.

- The vibrational energy takes two different transfer paths for noise propagation: 1) airborne contribution where the noise is directly radiated by the e-motor frame, and 2) structure-borne contribution due to the vibrations transmitted from the stator system to the car-body through its mountings. These sources are then combined with their respective measured transfer functions to get the interior noise contribution. As a reminder, in this work, only the structure-borne contribution is studied but the methodology developed can be used for airborne contribution as well.
- The airborne contribution and structure-borne contribution is combined to give the interior whining noise contribution and can be written as:

$$L(\omega) = 10 \log_{10} \frac{\langle |[\mathbf{H}^{\text{NTF}}(\omega)\mathbf{Q}(\omega)] \oplus [\mathbf{H}^{\text{VTF}}(\omega)\mathbf{F}(\omega)]|^2 \rangle}{p_{\text{ref}}^2}, \quad (5)$$

where, \oplus denotes the complex addition of airborne and structure-borne contributions, L is the sound pressure level [dB(A)] inside the cabin as complex function of frequency ω [Hz], \mathbf{H}^{NTF} corresponds to the measured noise transfer function in [Pa/(m³/s²)], \mathbf{Q} is the volume acceleration at the source location in [m³/s²], \mathbf{H}^{VTF} is the vibration transfer function in [Pa/N], \mathbf{F} in [N] is the excitation force applied on the car-body side, and p_{ref} is the reference sound pressure.

Estimation of natural frequencies and dynamic displacement of simplified stator system

The analytical approach is preferred to compute the natural frequencies of the stator system where the stator core, teeth, winding, and frame are modelled separately, as given in [3]. The simplified model assumes that the stator system behaves like a circular cylindrical shell, as shown in Figure 5, with clamped-clamped boundary conditions at its ends.

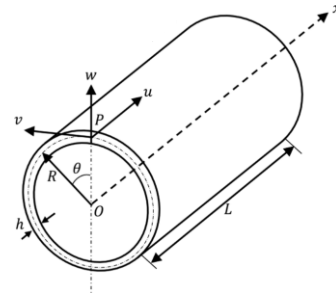


Figure 5. A thin circular cylindrical shell representing a simplified stator system [17]

Let $m \in \{0, 1, \dots, N_m\}$, $n \in \{1, \dots, N_n\}$ denote the circumferential and axial nodes of the simplified cylindrical shell, respectively. Then, the natural frequencies of the stator system can be approximated as:

$$f_{mn}^{\text{stat}} \approx \frac{1}{2\pi} \sqrt{\frac{K_m^{\text{core}} + K_{mn}^{\text{frame}} + K_m^{\text{winding}}}{M^{\text{core}} + M^{\text{frame}} + M^{\text{winding}}}} \quad (6)$$

where, K, M represent the calculated stiffness [N/m] and mass [kg] of each subsystem, respectively.

The amplitude of force acting on the stator of length L_s and internal radius R_{is} at the spatial order r can be written as:

$$\mathcal{F}_r(\omega) = 2\pi R_{is} L_s (|\hat{p}_r^{\text{rad}}(\omega)| + |\hat{p}_r^{\text{tan}}(\omega)|) \quad (7)$$

To compute the dynamic displacement of the simplified stator system, modal expansion can be used to estimate the displacement of the stator system with a finite number of spatial modes represented by N_k in each direction as:

$$\begin{aligned} \mathcal{U}_u^{\text{stat}}(x, \omega, \theta) &= \sum_{k=1}^{\infty} \alpha_k^{\text{stat}}(\omega) \tilde{\phi}_k^u(x, \theta) \\ &\simeq \sum_{k=1}^{N_k} \alpha_k^{\text{stat}}(\omega) \tilde{\phi}_k^u(x, \theta), \end{aligned} \quad (8)$$

$$\mathcal{U}_v^{\text{stat}}(x, \omega, \theta) \simeq \sum_{k=1}^{N_k} \alpha_k^{\text{stat}}(\omega) \tilde{\phi}_k^v(x, \theta), \quad (9)$$

$$\mathcal{U}_w^{\text{stat}}(x, \omega, \theta) \simeq \sum_{k=1}^{N_k} \alpha_k^{\text{stat}}(\omega) \tilde{\phi}_k^w(x, \theta) \quad (10)$$

where, x is the distance along the axial length, $\mathcal{U}_u^{\text{stat}}, \mathcal{U}_v^{\text{stat}}, \mathcal{U}_w^{\text{stat}}$ represent the displacement in axial, circumferential and radial direction, respectively and α_k is the modal participation factor for the vibration mode $\tilde{\phi}_k$.

The vibration modes are periodic along θ and therefore can be expanded using spatial-Fourier series [17,18]:

$$\tilde{\phi}_k^u(x, \theta) = \sum_{n=1}^{N_n} A_{mn} \phi_n'(x/L) e^{jm\theta}, \quad (11)$$

$$\tilde{\phi}_k^v(x, \theta) = \sum_{n=1}^{N_n} B_{mn} \phi_n(x/L) e^{jm\theta}, \quad (12)$$

$$\tilde{\phi}_k^w(x, \theta) = \sum_{n=1}^{N_n} C_{mn} \phi_n(x/L) e^{jm\theta}, \quad (13)$$

where, A, B, C are the constants as per [17], N_n represent the number of axial nodes considered, ϕ_n is the axial modal function and ϕ_n' represents its derivative with respect to the spanwise coordinate for a finite length cylindrical shell clamped at both ends. The axial modal function is given by:

$$\begin{aligned} \phi_n &= \cosh(\lambda_n x/L) - \cos(\lambda_n x/L) \\ &- \sigma_n (\sinh(\lambda_n x/L) - \sin(\lambda_n x/L)), \end{aligned} \quad (14)$$

where, λ_n and σ_n are the dimensionless beam-frequency parameters.

For airborne noise contribution, the equation for radiated power is readily available, refer [3]. Therefore, in this study, the focus is on propagation of uncertainties through structure-borne path. The structure-borne noise sources from e-powertrain vibration follow the transfer path from surface vibration of the frame of e-motor to the powertrain mounts and then from powertrain suspension to the vehicle body. In this work, this structure-borne noise contribution is realized using analytical and lumped parameters models. The input force acting on the car body is identified using a Stellantis internally developed MATLAB tool that acts as a transfer function when

provided with unit displacement at the outer surface of the motor. This can be represented by considering a linear time-invariant system whose dynamic behavior can be determined by the complex amplitude transfer function matrix \mathbf{H} relating to the vibration input (displacement/velocity/acceleration) \mathbf{X} , and the output forces \mathbf{F} . As a function of excitation frequency (ω),

$$\mathbf{H}_{MB}(\omega) = \frac{\mathbf{F}_B(\omega)}{\mathbf{X}_M(\omega)} \quad (15)$$

where, \mathbf{H}_{MB} is the transfer function matrix from mount to the car-body, \mathbf{F}_B is the force acting on the car-body due to the input vibration displacement (\mathbf{X}_M) from e-motor to mount.

Stochastic assessment of whining noise contribution

Steps to building stochastic metamodel to assess $L(\omega)$

- Sampling of operating conditions
- Determination of inputs and outputs for building the metamodel
- Sampling of relevant IPMSM design parameters based on prior domain-expert knowledge and literature review
- Develop a hierarchical Bayesian network indicating the dependencies along with hyper-parameters
- Posterior predictive distribution of the uncertain parameters and output responses
- Using the posterior samples to propagate the uncertainties from one model to another

Bayesian approach to metamodeling for uncertain inputs

In the literature, probabilistic metamodels based on Bayesian framework is particularly appealing due to the flexibility they provide in choosing the plausible design alternatives from the prior knowledge that has been acquired from previous experiences, measured data, and literature review, which provides an inherent regularization. In Bayesian context, the prior knowledge on the unknown random parameters θ are encoded in the form of a probability density function (pdf) given by $p(\theta)$. Let $p(\theta|\mathbf{y})$ denote the ‘‘full posterior’’ pdf of θ conditional on the observed data \mathbf{y} (either measured or simulated), then, using Bayes’ theorem [19],

$$p(\theta|\mathbf{y}) = \frac{f(\mathbf{y}|\theta)p(\theta)}{p(\mathbf{y})}, \quad (16)$$

where, $f(\mathbf{y}|\theta)$ represents the ‘‘likelihood’’ of observing the data given the parameters, and the denominator $p(\mathbf{y}) = \int_{\theta} f(\mathbf{y}|\theta)p(\theta)$ is the ‘‘evidence’’ of the observed data.

Typically, the denominator which acts as the normalization constant is difficult to compute due to intractability reasons and is ignored resulting in, $p(\theta|\mathbf{y}) \propto f(\mathbf{y}|\theta)p(\theta)$, which is solved generally using Markov chain Monte Carlo (MCMC) methods [20]. In this study, another sampler named No-U-Turn-Sampler (NUTS) based on Hamiltonian Monte Carlo is preferred due to its fast convergence and ability to autotune sampler parameters [21].

E-powertrain example case

The architectural details and important design parameters considered for the studied IPMSM are described in Table 1 and Table 2,

respectively. The macro-parameters chosen are same as the one studied in [22].

Table 1. IPMSM architecture details

Parameter		Nominal value
Number of pairs of poles (N_{pp})		4
Number of slots (N_s)		48
Stator phase number		3
Input current	Amplitude (I_0^{RMS})	250 A
	Phase angle (ϕ)	140°

Table 2. IPMSM geometrical design parameters

	Parameter	Nominal value [mm]
Stator	Outer radius (R_{os})	134.62
	Inner radius (R_{is})	80.95
	Stack length (L_s)	83.82
Frame	Outer radius (R_{of})	144
	Inner radius (R_{if})	136
	Length (L_f)	150
Magnet	Height (H_m)	6.5
	Length (L_m)	18.9
	Distance (D_m)	14

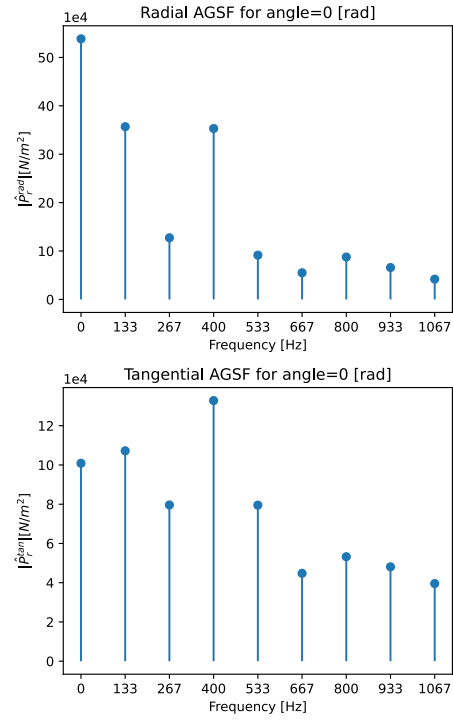


Figure 6. Radial (top figure) and Tangential (bottom figure) components of AGSF at 1000 RPM and across frequency given by: $2\nu f_e$ (or equivalently $2\nu N_{pp} f_m$, with $f_m = \frac{\Omega}{60}$ and $\nu = 0,1,2, \dots$)

As an example, Figure 6 shows the radial and tangential components of AGSF at spatial orders, $r = 2\nu N_{pp}$, where $\nu \in \{0,1,2, \dots\}$, when the 2D magnetic problem is solved using Pylecan at one specific operating condition (1000 RPM, 82 Nm). Applying the 2D Fourier transform, the spectrum of magnetic flux density and AGSF can be plotted. It can be clearly observed that radial AGSF is higher than the tangential AGSF at each harmonic. In this study, nevertheless, both radial and tangential components of AGSF are considered in an additive manner.

The natural frequencies of the nominal stator system is shown in Figure 7. The results show a good correlation from [3] for the same set of parameters adopted. It can be observed that the mode shapes with axial nodes $n > 1$ occur at higher frequencies. In this study, it is assumed that only the circumferential nodes ($m \in \{0,1, \dots, N_m\}$, $n = 1$) take part in generating noise.

It is to be noted that a high level of vibration and noise amplification is observed at two conditions: 1) coincidence of temporal frequency with the structural natural frequency i.e., $s f_e = f_{mn}^{stat}$, and 2) when the spatial order matches with circumferential structural node i.e., $r = m$.

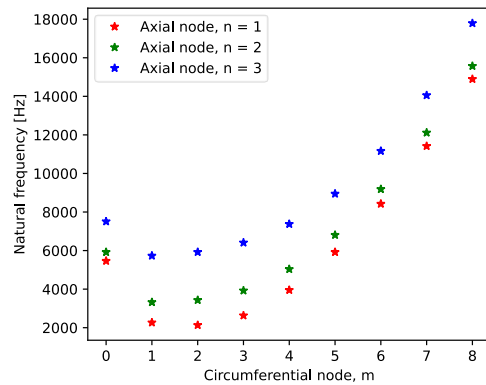


Figure 7. Natural frequencies of the stator system for different circumferential and axial node pairs (m, n)

Sampling of operating conditions (OC) as pairs of speed and torque (Ω, τ) is performed using the marginal probability law on real client usage profiles. Since the problem is not high-dimensional, a common inverse-transform sampling technique can be used to draw pairs of OC. The kernel estimated joint-distribution plot of the sampled pairs of OCs can be seen in Figure 8.

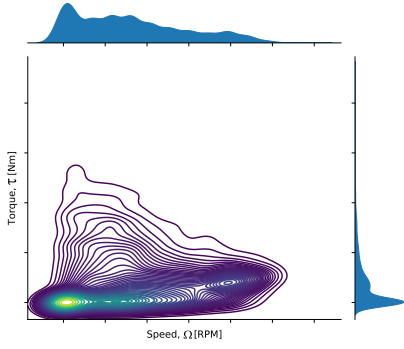


Figure 8. Joint distribution of the sampled OCs (Ω , τ). The two shaded curves at the edges represent the marginal distribution of the respective variable

The important IPMSM design parameters chosen for the stochastic study are listed in Table 2. The output AGSF (combination of radial and tangential components) can be computed for several e-machine configurations, however, looking at AGSF from Figure 9, it can be noticed that the input current phase angle affects the AGSF output significantly and therefore, it is important to consider ϕ in the input space.

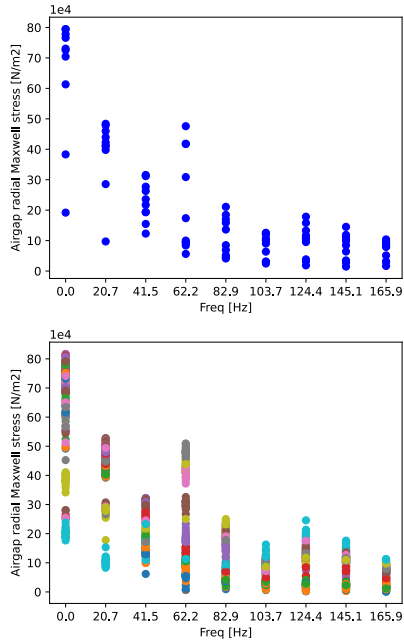


Figure 9. AGSF at one specific sampled speed (155 RPM), different phase angles and for one e-machine design (top figure), for multiple e-machine designs (bottom figure)

Metamodel to capture uncertainty in AGSF

To set up the domain of input variables, let $\mathbf{X} \in \mathbb{R}^{N_s \times n_p}$ be the matrix of predictor variables i.e., a collection of design parameters and the phase angle, where N_s , n_p denote the total number of observed samples and total number of predictor variables, respectively. Then, the input matrix can be written as, $\mathbf{X} = (\mathbf{L}_m, \mathbf{H}_m, \mathbf{D}_m, \mathbf{L}_s, \mathbf{R}_{os}, \mathbf{R}_{is}, \mathbf{L}_f, \mathbf{R}_{of}, \mathbf{R}_{if}, \phi)$. Except $\phi \in (0, \pi]$, each of these input design parameters ($\mathbf{x}_i \in \mathbb{R}^{N_s}$: $\mathbf{x}_i > 0$) are

considered random and are assumed to follow Inverse-gamma distributions whose support is $(0, \infty)$:

$$\mathbf{x}_i \sim \text{InvGamma}(a_i, b_i), \quad (17)$$

where, a, b are the hyper-parameters controlling the shape of the distribution.

With each of these parameters randomly chosen from the prior-distribution, it gives a notion of generating different e-machine designs parameterized with such macro-parameters. In this work, 20 different e-machine designs are generated. Looking at the Pearson's correlation coefficient plot in Figure 10, we notice that none of the parameters is highly correlated with one another and that the chosen input design domain is, indeed, pertinent indicating that the problem is well-posed.

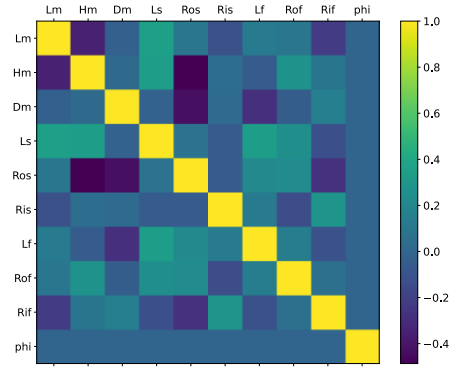


Figure 10. Pearson correlation matrix of IPMSM input parameters

Let $\mathbf{Y} \in \mathbb{R}^{N_s \times N_r}$ be the matrix of output responses such that each row vector $\mathbf{y}_i \in \mathbf{Y}$ corresponds to the AGSF at a specific spatial order r . These observed output responses are collected after simulating for each machine design at one specific OC, since only the frequencies at which AGSF acts, i.e., f_e depends on the OC and not on the amplitude of AGSF. Therefore, one metamodel to capture the distribution of unknown random parameters and responses is sufficient to infer the results at different harmonics. Moreover, before building a metamodel, the input-output data are divided into training and test dataset. The next step is to build a hierarchical Bayesian model on the training dataset in order to infer the distribution of unknown random parameters and responses. Once the parameters are inferred, they can be used to predict the posterior distribution on the unseen test dataset.

We can represent, generally, each observed (training) data

$\mathbf{y}_i(\omega) \in \mathbb{R}^{1 \times N_r}$ as:

$$\mathbf{y}_i(\omega) = f_i(\mathbf{X}, \boldsymbol{\alpha}) + \boldsymbol{\eta} \quad (18)$$

$$f_i(\mathbf{X}, \boldsymbol{\alpha}) = \boldsymbol{\alpha}_0 + \sum_{j=1}^{n_j} \boldsymbol{\alpha}_j \mathbf{X}_i^j \quad (19)$$

where, $\mathbf{X}_i \in \mathbb{R}^{n_p \times 1}$ is the predictor vector, \mathbf{X}^j represents each element in \mathbf{X} raised to power j , $\boldsymbol{\alpha}_0 \in \mathbb{R}^{1 \times N_r}$, $\boldsymbol{\alpha}_j \in \mathbb{R}^{N_r \times n_p}$ are the vectors of unknown coefficients, $\boldsymbol{\eta} \in \mathbb{R}^{1 \times N_r}$ is the vector of fitting errors consisting of modelling errors, n_j is the degree of the

polynomial, and $f_i(\mathbf{X}, \boldsymbol{\alpha})$ represents the surrogate function. For N_s training samples, the multivariate polynomial regression model can be represented as:

$$\mathbf{Y} = \tilde{\mathbf{X}}\boldsymbol{\theta} + \boldsymbol{\eta} \quad (20)$$

where, $\tilde{\mathbf{X}} = [\mathbf{1} \ \mathbf{X} \ \mathbf{X}^2 \ \dots \ \mathbf{X}^{n_j}] \in \mathbb{R}^{N_s \times (n_j n_p + 1)}$ is the augmented predictor matrix and $\boldsymbol{\theta} = [\boldsymbol{\alpha}_0 \ \boldsymbol{\alpha}_1 \ \boldsymbol{\alpha}_2 \ \dots \ \boldsymbol{\alpha}_{n_j}] \in \mathbb{R}^{(n_j n_p + 1) \times N_r}$ is the matrix containing the unknown coefficients.

In Bayesian modelling context, in this work, it is assumed that the observed (or computed,) data is distributed according to the Normal distribution with mean given by the surrogate function and variance σ_y^2 . Also, all the unknown random parameters follow respective prior-probability distributions, which are characterized by their own hyperparameters (which depends on the analyst's prior knowledge). Using the assumption of conditional independence, the full-joint probability can be represented using the directed acyclic graphs. This can be seen in Figure 11, where the observed random variables are represented using shaded regions and unknown random variables are represented using unshaded circles. Plate notation has been exploited to indicate the replication of random variables and that they are independently and identically distributed (i.i.d).

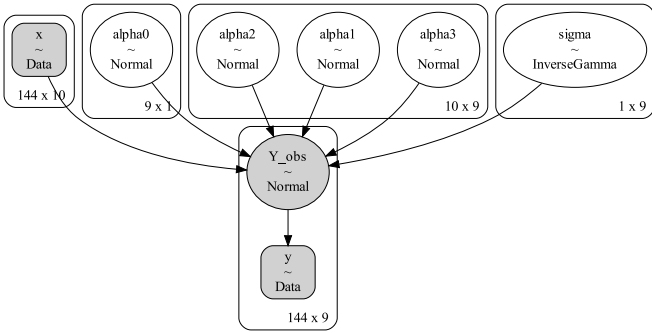


Figure 11. Hierarchical Bayesian model for AGSF (Y_{obs} is the likelihood)

The Bayesian model for AGSF simulated data with heteroscedastic¹ noise can be formulated as follows:

$$\begin{aligned} Y_{obs} | \mathbf{X}, \boldsymbol{\alpha}, \boldsymbol{\eta} &\sim \mathcal{N}(f(\mathbf{X}, \boldsymbol{\alpha}), \sigma_y^2), \\ \boldsymbol{\alpha}_0 &\sim \mathcal{N}(\mu_0, \sigma_0^2), \\ \boldsymbol{\alpha}_j &\sim \mathcal{N}(\mu_j, \sigma_j^2), \forall j = 1, \dots, n_j, \\ \sigma_y^2 &\sim \text{InvGamma}(\boldsymbol{a}_y, \boldsymbol{b}_y) \end{aligned} \quad (21)$$

The posterior predictive distribution, which is the distribution of the prediction on the unseen dataset according to $p(\boldsymbol{\alpha} | \mathbf{y}_{obs}, \mathbf{X}, \boldsymbol{\eta})$ is given by:

$$\begin{aligned} p(\mathbf{y}_{pred} | \mathbf{y}_{obs}, \mathbf{X}, \boldsymbol{\eta}) \\ = \int f(\mathbf{y}_{pred} | \boldsymbol{\alpha}, \mathbf{X}, \boldsymbol{\eta}) p(\boldsymbol{\alpha} | \mathbf{y}_{obs}, \mathbf{X}, \boldsymbol{\eta}) d\boldsymbol{\alpha} \end{aligned} \quad (22)$$

¹ Heteroscedasticity refers to the property of a dataset where the dispersion of the dependent variable (output response) around its mean is not constant along the space of independent variables.

The presented model is built in Python framework using open-source PyMC3 library. A total of 4 different MCMC chains were simulated resulting in 8,000 samples. The burn-in sample size (samples that are typically discarded during MCMC sampling, refer [19]) was set to 1,000 for each chain. The marginalized posterior distribution of each unobserved random parameter can be seen in Figure 12.

It can be observed that the 4 chains show a good mixing behaviour due to their unimodal distribution and the ranking of the chains being very close to unity. It indicates that each chain is sampling from the same distribution. This can also be confirmed using Gelman-Rubin statistic denoted by \hat{R} which should ideally be ≈ 1.0 as this measures the ratio of between-chains and within-chain variances [19]. For the current Bayesian model shown in Figure 11, $\hat{R} = 1.0$ for all random parameters. Moreover, the heteroscedastic modelling of noise, which assumes that the variance of noise varies across the input space, allows the model to be realistic which can be seen in the posterior predictive distribution of the output responses in Figure 13.

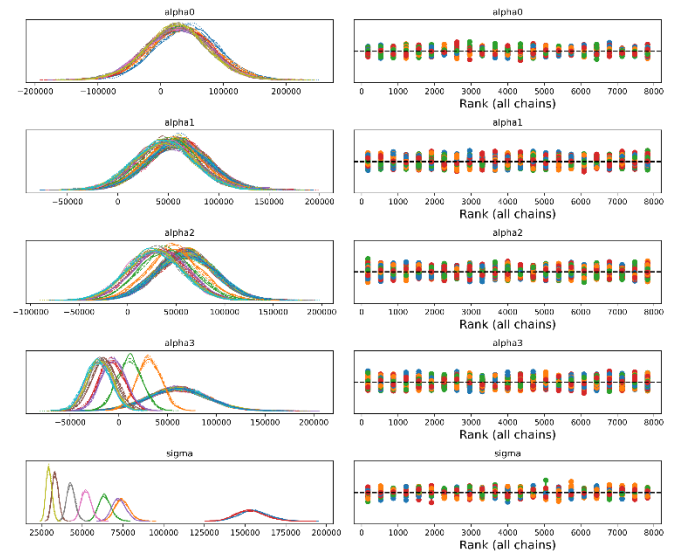


Figure 12. MCMC convergence results for the Bayesian model. Left column is the smoothed kernel density estimate (KDE) plot corresponding to each random variable and the right column consists of the rank plots

The posterior predictive distribution of AGSF when the test input data is used can be seen in Figure 13. At each frequency point, the distribution of the AGSF from all posterior samples can be observed. Typical Box-and-whisker plot (shown in black) describes the spread and median of the data with quartiles. The outliers fall above and below the whiskers. As the posterior sample space was abundant with 8,000 samples, the median and mean coincides indicating that the distribution at each frequency point is symmetric. In order to visualize this distribution, kernel density estimate is used to compute the empirical distribution of the sample (at each frequency point) with the help of violin plots (shown in blue). It can be seen that the inter-quartile range (IQR) at $(0, 0f_e)$ corresponding to 0 Hz and $(24, 6f_e)$ corresponding to 62.2 Hz is higher than at other frequency points and that for higher order harmonics the spread in AGSF levels is fairly low, considering the prior-expert knowledge used during the Bayesian modelling process.

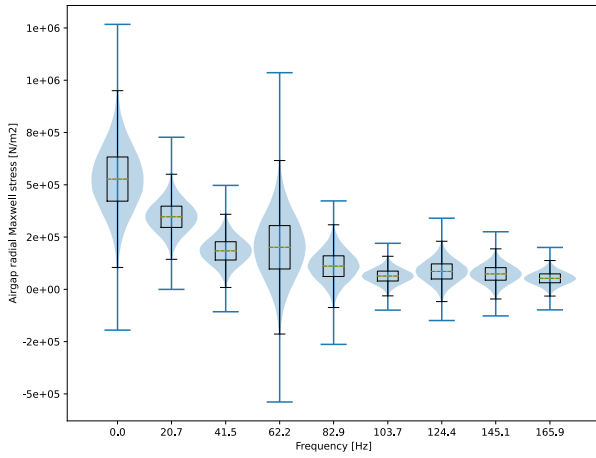


Figure 13. Posterior predictive distribution of the output response (AGSF) with respect to the unseen test dataset. Mean and median at each frequency point is shown with a horizontal line (blue-solid for mean and orange-dashed for median).

The output AGSF from different e-machine designs will now be propagated through structure-borne path. With the help of detailed FE modelling using commercial tools, this transmission of vibrational energy from electric motor's frame to the mounts and to the vehicle body can be achieved (refer [15]). However, during stochastic modelling several random samples need to be evaluated and therefore, analytical models seem to be the best choice trading the accuracy with time-efficiency. In the next section, a typical e-powertrain system is considered and analytical displacements coming from motor frames are imposed on it.

Metamodel to capture uncertainty in structure-borne contribution

For structure-borne noise contribution, the vibration displacement at the surface of the motor needs to be estimated. These vibrations are transmitted through e-powertrain mounts to the car-body. Figure 14 shows a schematic to estimate the displacement and the input forces acting on the car-body. Such a model consists of lumped parameters and multiple rigid (components mounted on, for instance, one crossbeam) and flexible bodies (rubber mounts) representing the powertrain mounting system.

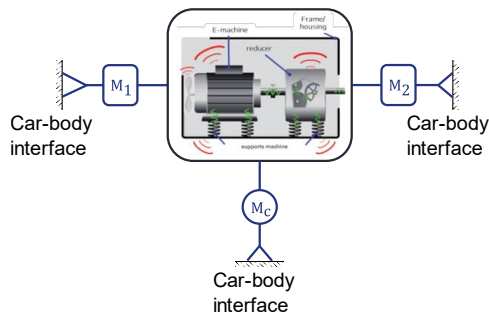


Figure 14. A schematic showing the transfer of vibrations from e-motor's surface to powertrain mounts (M_1 : left mount, M_2 : right mount, and M_c : connection to the cradle point) and then to the car-body

In this work, an internal Stellantis tool developed in MATLAB is used to estimate the forces, where it is assumed that the vibrational

energy from the motor surface is transmitted linearly to the mounts on the e-powertrain side. Therefore, here it is assumed sufficient to approximate the displacement using (8)-(10) at each mount and in every direction.

However, observing some measured data from one of the classical systems (see Figure 15), it is clear that there is no distinct pattern in the level of displacements acting on each powertrain mount and that there is no dominant direction of displacement. On the other hand, observing the displacements on the same data with respect to different orders which indicates that dominant harmonics can indeed be identified and should be the basis of further investigation. In this view, the root-mean-squared (RMS) values of displacement considering a simplified cylindrical shell model can be estimated from equations (8)-(10) as shown below:

$$U_{\text{RMS}}^{\text{stat}} = \sqrt{\frac{1}{\Omega_s} \sum_{s=1}^{\Omega_s} [(U_{us}^{\text{stat}})^2 + (U_{vs}^{\text{stat}})^2 + (U_{ws}^{\text{stat}})^2]} \quad (23)$$

where, Ω_s is the total number of speed profiles sampled in RPM.

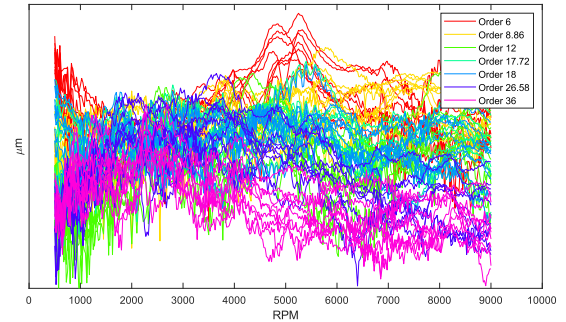


Figure 15. Vibration displacement measured data on all 3 mounts and in all directions plotted together. Dominant harmonics can be identified, for instance, at $\Omega=5000$ RPM, spatial order 6 is the most dominant source of displacement.

Figure 16 shows the RMS displacement at each spatial order. As expected, the displacement at ($r = 0$) is maximum for small RPMs and remains constant throughout (time invariant deformation) and therefore, the vibration velocity induced will be negligible. In spite of some distinct peaks that can indeed be observed around 1.4 kHz, the vibration velocity exhibits a rather monotonic behavior at low frequencies below 1.4 kHz as a result of simplified formulation. Also, the maximum displacement occurs when the current phase angle $\phi = 140^\circ$ which corresponds to MTPA condition (maximum torque per ampere). Note that the pattern of displacement is different from the measured data (Figure 15) due to the fact that the measured data is on a different e-machine architecture and is used as a prior knowledge for the simplification of analytical models.

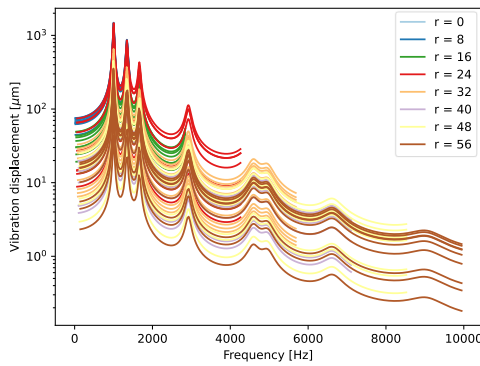


Figure 16. Vibration RMS displacement on the motor surface for one specific e-machine design, multiple OCs and multiple current phase angles.

Body input force identification

Due to the scarcity of measured data, the vibration displacement at the surface of the motor is estimated using analytical approach as shown in the previous section. Next, the forces acting on the car-body ($F_B(\omega)$) due to the e-powertrain vibration needs to be estimated so that they can be coupled with the measured vehicle vibration transfer function ($H^{VTF}(\omega)$) to get the interior cabin SPL. This is shown in the form of a simple flowchart in Figure 17.

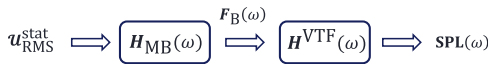


Figure 17. Flowchart depicting the points where the structure-borne quantities are coupled with the respective transfer functions

First, the transfer function $H_{MB}(\omega)$ is identified by providing a unit excitation to each mount and in each direction, using the internally developed tool. As an example, for a particular spatial order $r = 8$, the identified transfer functions for the left mount due to unit excitation is shown in Figure 18. It is to be noted that the transfer functions are obtained for each direction and for all three mounting positions, the schematic for which is depicted in Figure 14.

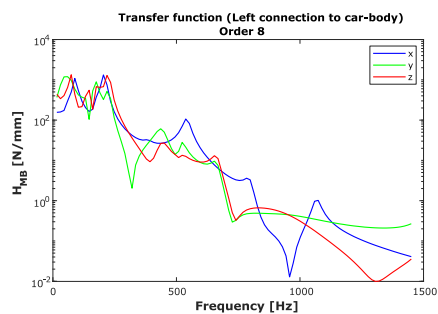


Figure 18. Transfer functions from the developed MATLAB routine with unit excitation to the left mount in all three directions for one specific spatial order

The force responses due to true RMS displacements (u_{RMS}^{stat}) for each e-machine design can then be recomposed using the identified $H_{MB}(\omega)$. The recomposed forces ($F_B(\omega)$) acting on the car-body through left mount bracket side is shown, as an example, in Figure 19. It can be observed that there exists a significant level of variability in the forces acting in all three directions when all the e-

machine configurations were considered along with different input current phase angles.

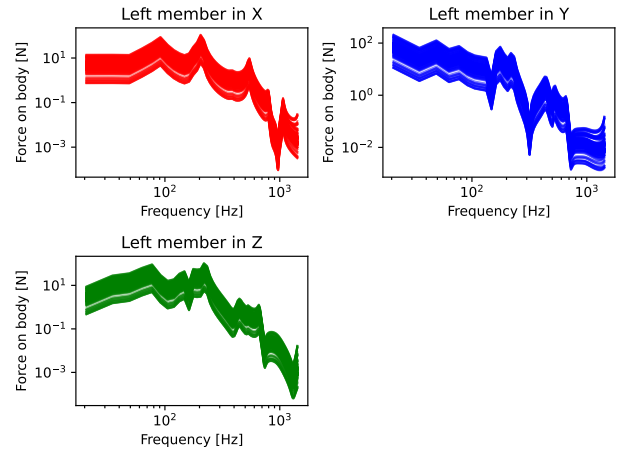


Figure 19. Forces acting on the car-body through left mount bracket in different directions for order 8 considering all e-machine designs and current phase angles

Vehicle transfer functions to the interior cabin

The measured set of transfer function database consists of vibration transfer function (VTF) and noise transfer function (NTF). Structural-acoustic measurements procedures make use of the reciprocity principle, where the excitation is produced by an acoustic source placed at driver's ear location inside the internal acoustic cavity and acceleration responses are measured on selected degrees of freedom. In this study, VTF measured from 9 input points (3 mount locations and 3 directions) in the frequency range [20, 2048] Hz were considered. For instance, Figure 20 shows VTF measured from 3 input points of left mount bracket to the interior cabin's left front seat.

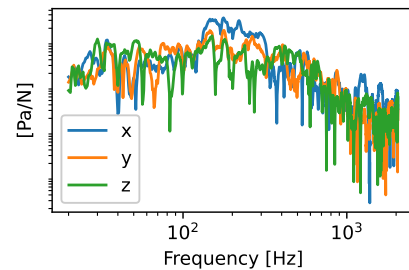


Figure 20. Measured vehicle transfer functions from left mount bracket to left front seat mean.

Interior SPL structure-borne contribution

To get the interior SPL contribution due to structure-borne phenomenon, the obtained set of forces acting on the car body through each mount and in each direction (Figure 19) is multiplied with the respective vehicle transfer function (Figure 20).

In Figure 21, we can see the dispersion in interior sound pressure level due to variation in machine design and current phasing over the operating speed samples. It should be noted here that this plot is strictly for the noise transmitted by the left mount bracket in x-

direction. Similarly, the contribution coming from different mounts and in different directions can be obtained and combined together to produce the whining noise contribution due to SBN path.

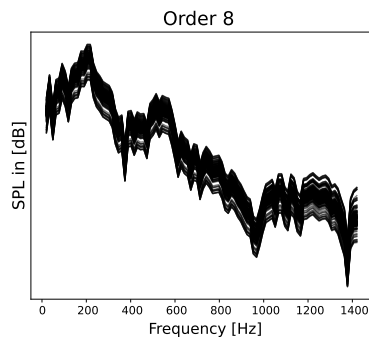


Figure 21. Interior SPL from left front bracket considering all machines and all current phase angles

To quantify the uncertainties associated with the output SPL, a similar approach as shown for AGSF can be performed which would give the posterior samples of SPL conditional on the observed data. For each frequency point, a kernel density estimate can be plotted indicating the 95% credible interval as shown in Figure 22. It shows the contribution to interior SPL from left mount bracket in all three directions as well as the combined contribution in the fourth plot. Here, the variability in the output responses is due to design matrix that we considered which had random geometrical macro-parameters as well as the different current phase angles. This is useful as it implies that the uncertainty in the output responses does not consider the uncertainty in the measured transfer functions. Indeed, stochasticity in transfer functions can be induced using the data measured on different vehicles which will be a part of future works.

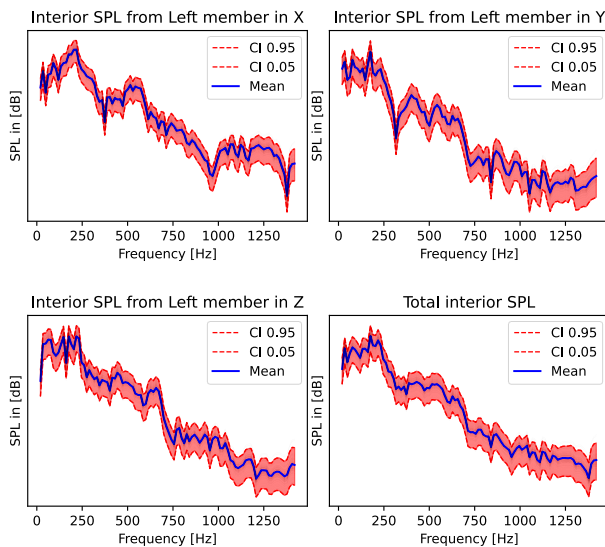


Figure 22. Kernel density estimate plot of interior SPL at each frequency point for spatial order 8 considering the left mount bracket

Conclusions & Perspectives

In this study, a typical workflow from deterministic to stochastic analysis of e-powertrain whining noise contribution is developed. During the early design stage, deterministic methods would not be helpful as detailed designs are not available. Hence, the probabilistic methods, developed in this work, help to compensate this lack of knowledge. A stochastic metamodeling approach within Bayesian framework is presented in order to quantify the uncertainties in geometrical macro-parameters and operating conditions. The developed Bayesian model is based on multivariate polynomial basis expansion with heteroscedastic noise. It has been employed more specifically here to obtain the posterior predictive distributions of electromagnetic forces within the airgap. Semi-analytical models have been realized to determine the sound pressure level inside the cabin using the measured transfer functions. It is noticed that kernel density estimates provide an efficient way to understand the spread of the output responses due to uncertain inputs. Specific uncertainties in the measured transfer functions database will be investigated in the future works through various dimensionality reduction approaches.

In a nutshell, using the probabilistic approach described here on a specific system and given the macro-parameters at the early-design stage of an electric vehicle, the interior SPL dispersion can be estimated by an NVH designer and help prioritize the suitable noise mitigation techniques that can be employed.

References

1. Bibra, E.M., Connelly, E., Gorner, M., Lowans, C., Paoli, L., Tattini, J., and Teter, J., "Global EV Outlook 2021: Accelerating Ambitions Despite the Pandemic," 2021.
2. Qian, K., Wang, J., Gao, Y., Sun, Q., and Liang, J., "Interior noise and vibration prediction of permanent magnet synchronous motor," *Journal of Vibroengineering* 20(5):2225–2236, 2018.
3. Gieras, J.F., Wang, C., and Lai, J.C., "Noise of polyphase electric motors," CRC press, ISBN 1-315-22098-9, 2018.
4. Deng, W. and Zuo, S., "Electromagnetic Vibration and Noise of the Permanent-Magnet Synchronous Motors for Electric Vehicles: An Overview," *IEEE Trans. Transp. Electrific.* 5(1):59–70, 2019, doi:10.1109/TTE.2018.2875481.
5. Vijayraghavan, P., "Noise in Electric Machines: A Review," *IEEE TRANSACTIONS ON INDUSTRY APPLICATIONS* 35(5):8, 1999.
6. Blanning, R.W., "The construction and implementation of metamodels," *SIMULATION* 24(6):177–184, 1975, doi:10.1177/003754977502400606.
7. Wang, G.G. and Shan, S., "Review of Metamodeling Techniques in Support of Engineering Design Optimization," *Journal of Mechanical Design* 129(4):370–380, 2007, doi:10.1115/1.2429697.
8. Wang, B., Rahman, T., Chang, K., Mohammadi, M.H., and Lowther, D.A., "A neural network based surrogate model for predicting noise in synchronous reluctance motors," *2016 IEEE Conference on Electromagnetic Field Computation (CEFC)*, 1–1, 2016, doi:10.1109/CEFC.2016.7816297.
9. Mohammadi, M.H., Rahman, T., Silva, R.C.P., Wang, B., Chang, K., and Lowther, D.A., "Effect of Acoustic Noise on Optimal SynRM Design Regions," *IEEE Trans. Magn.* 54(3):1–4, 2018, doi:10.1109/TMAG.2017.2760859.
10. Ibrahim, I., Silva, R., Mohammadi, M.H., Ghorbanian, V., and Lowther, D.A., "Surrogate-Based Acoustic Noise Prediction of

Electric Motors,” *IEEE Transactions on Magnetics* 56(2):1–4, 2020, doi:10.1109/TMAG.2019.2945407.

11. Jeannerot, M., Dupont, J.-B., Sadoulet-Reboul, E., Ouisse, M., Lanfranchi, V., and Bouvet, P., “Design of silent electric motors: optimization under constraints and parameters uncertainties,” *2020 International Conference on Electrical Machines (ICEM)*, 429–435, 2020, doi:10.1109/ICEM49940.2020.9271056.
12. Beltrán-Pulido, A., Aliprantis, D., Bilionis, I., Munoz, A.R., Leonardi, F., and Avery, S.M., “Uncertainty Quantification and Sensitivity Analysis in a Nonlinear Finite-Element Model of a Permanent Magnet Synchronous Machine,” *IEEE Transactions on Energy Conversion* 35(4):2152–2161, 2020, doi:10.1109/TEC.2020.3001914.
13. Prakash, V., Sauvage, O., Antoni, J., and Gagliardini, L., “Bayesian NVH metamodels to assess interior cabin noise using measurement databases,” *Proceedings of the 30th International Conference on Noise and Vibration Engineering, ISMA*, 1666–1684, 2022.
14. Bonneel, P., Le Besnerais, J., Pile, R., and Devillers, E., “Pyleecan: an open-source Python object-oriented software for the multiphysic design optimization of electrical machines,” *2018 XIII International Conference on Electrical Machines (ICEM)*, IEEE, ISBN 1-5386-2477-X: 948–954, 2018.
15. Dupont, J.-B., Bouvet, P., and Wojtowicki, J.-L., “Simulation of the airborne and structure-borne noise of electric powertrain: Validation of the simulation methodology,” SAE Technical Paper, ISBN 0148-7191: 2013-01–2005, 2013.
16. Gieras, J.F., Wang, C., Joseph, C.L., and Ertugrul, N., “Analytical prediction of noise of magnetic origin produced by permanent magnet brushless motors,” *2007 IEEE International Electric Machines & Drives Conference*, IEEE: 148–152, 2007.
17. Blevins, R.D. and Plunkett, R., “Formulas for natural frequency and mode shape,” *Journal of Applied Mechanics* 47(2):461, 1980.
18. Leissa, A.W., “Vibration of Shells,” Scientific and Technical Information Office, National Aeronautics and Space Administration, 1973.
19. Gelman, A., Carlin, J.B., Stern, H.S., and Rubin, D.B., “Bayesian data analysis,” Chapman and Hall/CRC, ISBN 0-429-25841-0, 1995.
20. Bolstad, W.M. and Curran, J.M., “Introduction to Bayesian statistics,” John Wiley & Sons, ISBN 1-118-09156-6, 2016.
21. Hoffman, M.D. and Gelman, A., “The No-U-Turn Sampler: Adaptively Setting Path Lengths in Hamiltonian Monte Carlo,” 31.
22. Yang, Z., Krishnamurthy, M., and Brown, I.P., “Electromagnetic and vibrational characteristic of IPM over full torque-speed range,” *2013 International Electric Machines & Drives Conference*, IEEE, Chicago, IL, USA, ISBN 978-1-4673-4974-1: 295–302, 2013, doi:10.1109/IEMDC.2013.6556267.

Contact Information

Vinay Prakash,
Stellantis N.V., Automotive research and advanced engineering,
2 Bd de l’Europe, 78300 Poissy, France
Email: vinay.prakash@stellantis.com

Acknowledgments

This research work is funded by the European Commission’s H2020-Innovative training network (ITN) under the project ECODRIVE (Grant Nr. 858018) and we gratefully acknowledge the support of OpenLab Vibro-Acoustic-Tribology@Lyon, Laboratoire Vibrations Acoustique (LVA), INSA Lyon and the NVH department of Stellantis N.V.

Definitions/Abbreviations

NVH	Noise, vibration and harshness
EV	Electric vehicle
IPMSM	Interior permanent magnet synchronous motor
OC	Operating condition
SPL	Sound pressure level
EM	Electromagnetic
AGSF	Airgap surface force
pdf	Probability density function
KDE	Kernel density estimate
MCMC	Markov Chain Monte Carlo
VTF	Vibration transfer function
NTF	Noise transfer function